Spatial-angular compounding for elastography using beam steering on linear array transducers

Min Rao, Quan Chen, and Hairong Shi
Department of Medical Physics, The University of Wisconsin-Madison, 1300 University Avenue, 1530 MSC, Madison, WI 53706

Tomy Varghese[a)]
Department of Medical Physics and Department of Biomedical Engineering, The University of Wisconsin-Madison, 1300 University Avenue, 1530 MSC, Madison, WI 53706

(Received 24 June 2005; revised 5 November 2005; accepted for publication 4 January 2006; published 9 February 2006)

Spatial-angular compounding is a new technique that enables the reduction of noise artifacts in ultrasound elastography. Under this method, compounded elastograms are obtained from a spatially weighted average of local strain estimated from radio frequency (rf) echo signals acquired at different insonification angles. In previous work, the acquisition of the rf signals was performed through the lateral translation of a phased-array transducer. Clinical applications of angular compounding would, however, require the utilization of beam steering on linear-array transducers to obtain angular data sets, which is more efficient than translating phased-array transducers. In this article, we investigate the performance of angular compounding for elastography by using beam steering on a linear-array transducer. Quantitative experimental results demonstrate that spatial angular compounding provides significant improvement in both the elastographic signal-to-noise ratio and the contrast-to-noise ratio. For the linear array transducer used in this study, the optimum angular increment is around 1.5°–3.75°, and the maximum angle that can be used in angular compounding should not exceed 10°. © *2006 American Association of Physicists in Medicine*. [DOI: 10.1118/1.2168429]

Key words: angular compounding, angled beams, compounding, elastography, elastogram, elasticity, elasticity imaging, strain, stiffness, signal-to-noise, ultrasound

I. INTRODUCTION

In recent years, tissue elasticity imaging has received considerable interest for the diagnosis of disease.[1–14] It is well known that many diseases are associated with alterations in tissue stiffness. However, this change in stiffness is not detectable under a standard ultrasound examination since the echogenicity and stiffness of tissues are caused by unrelated mechanisms and are thus uncorrelated.[3] Elastography is an imaging modality that is capable of mapping local internal strains that a tissue experiences after a quasistatic compression. In this technique, local displacements are typically computed by applying cross-correlation analysis to the pre- and postcompression ultrasonic radio frequency (rf) echo signals. Strains are then estimated as the gradient of the displacements along the beam axis and displayed as an image referred to as an elastogram.

Tissue compression distorts the postcompression signal, leading to echo signal decorrelation. Signal decorrelation noise is one of the major limiting factors in strain estimation and imaging.[3,4] Many algorithms have been developed to reduce decorrelation noise and to improve the elastographic signal-to-noise ratio (SNR_e), such as temporal stretching,[15–17] multicompression averaging,[18] wavelet denoising,[19] and other compounding approaches.[20,21] Temporal stretching of the postcompression signal by the appropriate factor can compensate for axial decorrelation effects. The stretching operation may be global or adaptive.[15–17] Global stretching requires *a priori* knowledge of the applied compression and works most effectively for homogeneous and uniformly elastic media. Adaptive stretching, on the other hand, is more suitable when imaging inhomogeneous media because it adaptively varies the stretching factor according to the local tissue strain.[15] However, it is computationally intensive when compared to global stretching. Multicompression averaging reduces decorrelation by averaging elastograms generated using successive small compressions.[18] Wavelet denoising smoothes the displacement estimates in the wavelet domain without losing edge information.[19] Most of these algorithms can be used in conjunction with each other for artifact reduction in elastography.

Spatial-angular compounding for elastography was recently introduced by Techavipoo *et al.*[22,23] to reduce noise artifacts in elastograms. Spatial-angular compounding averages multiple strain estimates around the same region-of-interest (ROI) acquired from different insonification angles. This technique utilizes the same concept utilized to reduce speckle noise[24] in conventional US imaging with angular compounding of the *B*-mode signals.[25–27] *B*-mode angular compounding has been used and implemented on commercial ultrasound scanners. The results presented by Techavipoo[22,23] illustrate the improvement in the SNR_e and elastographic contrast-to-noise ratio (CNR_e) obtained with angular compounding. In that work, however, rf echo signals at different angular insonification directions were acquired

by translating a phased-array ultrasound transducer in the lateral direction, which is time consuming and subject to measurement errors due to transducer positioning. Another disadvantage of using phased-array transducers is that the data sets need to be rearranged during off-line analysis so that the A lines along the same angle from all the sector images can be grouped together to form rf frames at that specified angle. Clinical application of angular compounding, however, would require the utilization of beam steering on linear-array transducers to directly obtain the angular data sets, which is more efficient and accurate than translating phased-array transducers.

In this article, we investigate the performance of spatial-angular compounding for elastographic imaging using beam steering on a linear-array transducer. A unidirectional, quasistatic compressional force is applied, and pre- and postcompression rf echo signals are acquired at different beam steering angles. Angular elastograms estimated at the different angles are weighted and then averaged to generate a compounded elastogram. We present results obtained using both uniformly elastic and single inclusion phantoms that demonstrate the improvements in the elastographic SNR_e and CNR_e. We also examine the use of global temporal stretching in conjunction with spatial-angular compounding.

II. MATERIALS AND METHODS

Improvements in the elastographic SNR_e and CNR_e obtained using spatial-angular compounding were assessed using a uniformly elastic phantom of size $10\times10\times10$ cm^3 and a single-inclusion phantom of size $9\times9\times9$ cm^3, respectively. Both phantoms were manufactured in our laboratory.[28] The inclusion phantom contains a 1 cm diameter cylindrical inclusion encased within a uniform background. The inclusion was three times stiffer than the background.

Both phantoms were scanned using an Ultrasonix 500RP (Ultrasonix Medical Corporation, Bothell, WA, and Vancouver, BC, Canada) real-time scanner equipped with a 5 MHz linear-array transducer with an approximate 60% bandwidth. In order to acquire rf data at different beam angles, we developed an ultrasound research interface (URI) client program, to communicate with the Ultrasonix URI and software server and control the beam steering algorithm. The URI client program enables the operator to input the maximum angle and the angular increment, and the system will automatically scan the phantom along the specified angular sweep. In our experiment, the phantoms were scanned from $-15°$ to $15°$ with a minimum angular increment of $0.75°$.

A compression plate with a rectangular slot fitted with the transducer was mounted on a linear stage driven by a stepper motor. The compression plate is larger than the phantom surface, providing uniform compression of the phantom, as shown in Fig. 1. The compression was applied along the axial direction, i.e., angle $0°$, without beam steering. Echo signals were acquired, originating from the depth of 1.5 cm in the phantom to the depth of 5.5 cm, before and after a compression of 0.5% of the phantom height. The stepper motor controlled compression of the phantom is also controlled by the URI client program on the Ultrasonix 500RP system. The program controls the stepper motor apparatus that enables synchronized acquisition of both pre- and postcompression rf data sets after the quasistatic compression. We have implemented an automated beam steering and data acquisition algorithm on the Ultrasonix system. The algorithm first acquires the precompression data along the specified angular sweep $(-15°-15°)$ at $0.75°$ increments. The stepper motor is then activated to compress the phantom at a specified compression increment (0.5%), following which the postcompression rf data set is acquired following the same angle sequence. In order to obtain statistically useful results, pre- and postcompression data were acquired over eight independent realizations within the same scanning plane but at different precompression levels.

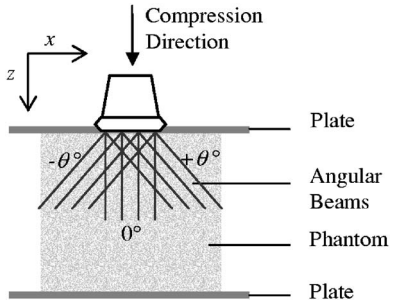

FIG. 1. A schematic diagram for elastographic imaging using a linear array transducer with beam steering. The z and x directions are defined as the axial and lateral direction of the ultrasound beam without beam steering.

Each of the angular pre- and postcompression rf frames acquired were analyzed separately to generate an elastogram at the specified angle, referred to as an angular elastogram. Angular elastograms were computed using the following procedure. A cross-correlation algorithm using a window size of 3 mm and 75% overlap of consecutive windows was used to generate displacement estimates. A five-point, one-dimensional median filter was then applied to eliminate the outliers in the displacement estimates. A three-point, least squares strain estimator[29] was used to generate local strain estimates. Angular elastograms were finally filtered using a 5×5 median filter to suppress strain outliers.

Compound-elastograms were obtained by weighted averaging over different angular increments $(\Delta\theta)$ and numbers of angular elastograms (N). The strain estimate computed for each image or pixel location is given by[22,23]

$$C(\Delta\theta,N)=\frac{1}{N}\sum_{i=-n}^{n} w_x(\nu,i\Delta\theta)A(i\Delta\theta), \tag{1}$$

where $C(\Delta\theta,N)$ represents a compound elastogram. N is the number of angular elastograms used in compounding, which equals $2n+1$, where n is the number of angular elastograms in either the positive or negative angular direction. $A(\theta)$ and $w_x(\nu,\theta)$ are the angular elastogram and the weighting factor for axial strains at angle θ, respectively. The weighting factor is given by[22,23]

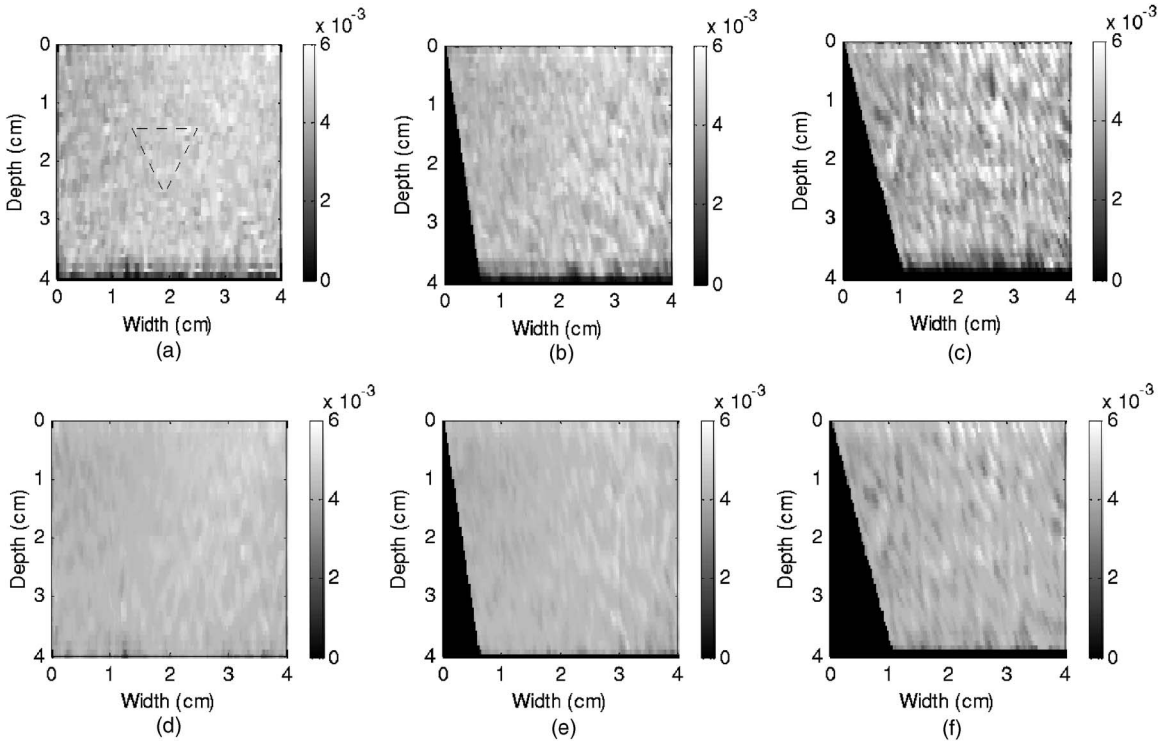

FIG. 2. Angular elastograms of the uniformly elastic tissue-mimicking phantom. The first row illustrates elastograms without global temporal stretching while the second row shows those with global temporal stretching. The first, second, and third columns show elastograms obtained at 0°, 9°, and 15° insonification angles, respectively. The colorbar denotes strain, where a 1% strain is displayed as 0.01.

$$w_x(\nu,\theta) = 1/(\cos^2\theta - \nu\sin^2\theta), \tag{2}$$

where ν is the Poisson's ratio, which is assumed to be 0.495 for incompressible soft tissue.[30] As described in our previous work,[23] each angular elastogram needs to be spatially registered such that the pixels of each angular elastogram lie on the same rectangular grid. Bilinear interpolation was used to perform the spatial registration in this article.

To compare experimental results obtained using the linear-array transducer to that of the phased-array transducer, the same angular increment values (0.75°, 1.5°, 3.75°, and 7.5°) were applied. Again, only cases where compounding of both symmetrical positive and negative angles were considered. For our linear-array transducer, however, the maximum angle to apply beam steering was limited to ±15° instead of the ±45° available with the phased-array transducer.

The values of elastographic SNR_e were analyzed for angular and compound elastograms of the uniform phantom. The SNR_e is defined as[31]

$$\mathrm{SNR}_e = \frac{\bar{s}}{\sigma_s}, \tag{3}$$

where $\bar{s}$ and σ_s are, respectively, the mean and standard deviation of the strains over pixels in the common region. For the inclusion phantom, the values of the strain contrast C_0 and the CNR_e were analyzed for both noncompounded and compound elastograms. The strain contrast C_0 and the elastographic CNR_e are defined as follows:[32]

$$C_0 = s_2/s_1, \tag{4}$$

$$\mathrm{CNR}_e = \frac{2(s_1 - s_2)^2}{(\sigma_1^2 + \sigma_2^2)}, \tag{5}$$

where s and σ^2 are the mean and variance of the strains in the selected ROI. Subscripts 1 and 2 refer to the regions inside and outside the inclusion, respectively. For both phantoms, we acquired eight sets of pre- and postcompression rf data along the same imaging plane of the phantom using different precompression levels, to obtain statistical results for the SNR_e and CNR_e estimates.

III. RESULTS

A. Uniform phantom

Figure 2 presents examples of angular elastograms before appropriate weighting, obtained from the uniformly elastic phantom, for angles of 0°, 9°, and 15°. The first row illustrates elastograms without global temporal stretching and the second row shows those with global temporal stretching. As expected, we observe increased noise artifacts in the strain images at larger insonification or beam angles. This is due to the fact that angular elastograms obtained where the beam angle relative to the direction of compression is large, suffer from significant decorrelation of the pre- and postcompression rf echo signals due to the movement of the scatterers. Note also that the angular elastograms become darker as the angle increases, suggesting that the strains measured at larger

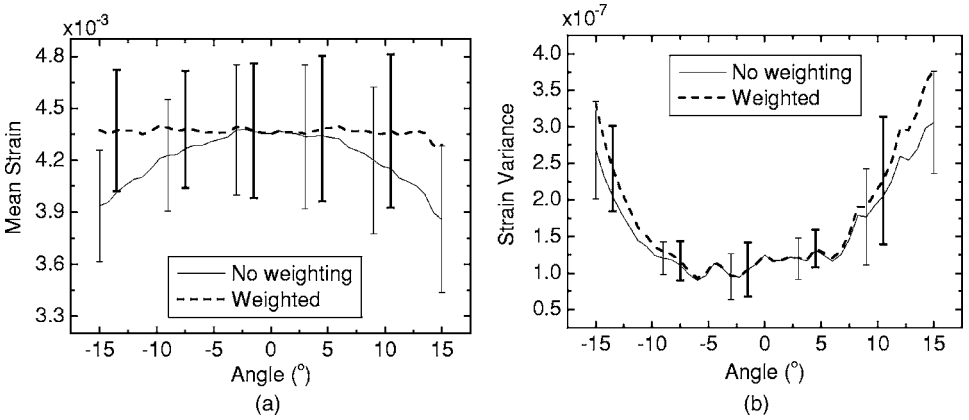

FIG. 3. Mean strain (a) and strain variance (b) with the standard deviation plotted as error bars over eight independent data sets vs beam steering angle. Strain estimates obtained with weighting (thick dashed line) and without weighting (light solid line) are depicted. Elastograms were obtained without global temporal stretching. The mean and variance of strain estimates were computed over the triangular region shown on the elastogram in Fig. 2(a).

angles are biased lower than those measured at smaller angles. This bias is compensated by appropriate angular weighting of the angular strain estimates.

Figure 3 shows the mean and variance of strains in the elastograms obtained at different beam steering angles without global stretching. Mean and variance of strain estimates were computed over the triangular region shown on the elastogram in Fig. 2(a). Mean and variance values are presented with (thick dashed line) and without (light solid line) angular weighting to obtain the axial strain estimates. The error bars represent the standard deviation of the mean estimates obtained over eight independent experiments. Without angular weighting, the observed strain at each beam direction varies with angle. After weighting is applied, we obtain the strain component along the axial direction that is independent of the beam angle. As expected, the variance of the strain increases at larger angles, as shown in Fig. 3(b). Angular weighting magnifies the variance, especially for larger angles. The results with global temporal stretching are not shown here since they show a similar trend regarding the dependence on the beam steering angles except at lower values of strain variance.

The SNR_e in the angular elastograms obtained at different beam steering angles are shown in Fig. 4. The results with global temporal stretching (thick dashed line) are compared to that without stretching (light solid line). The two curves have a similar trend, with decreased SNR_e at the larger insonification angles. We observe an increase in SNR_e with temporal stretching because the decorrelation noise artifacts have been further reduced. Note that the curves are not exactly symmetric with the 0° beam angle, but are much better than the results of the phased-array transducer presented by Techavipoo *et al.*[22,23] This slight asymmetry more likely arises from measurement uncertainty, rather than due to the asymmetry among the beams transmitted by the linear-array transducer.

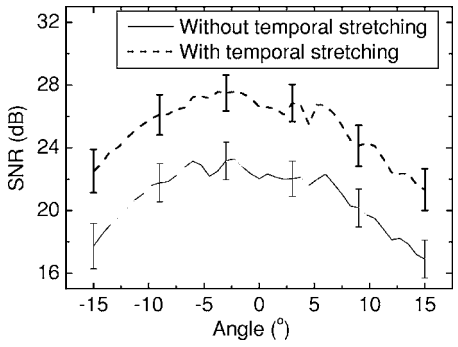

FIG. 4. Variation in the elastographic SNR_e vs beam angle for the eight independent data sets, with the standard deviation plotted as error bars.

Compound elastograms are shown in Fig. 5, using a 1.5° angular increment with a maximum angle of 10.5° and 15°, respectively. The first row shows compound elastograms obtained without temporal stretching. The second row shows compounded elastograms obtained using global temporal stretching. The region demarcated by the two dashed lines on the elastogram represent locations for which strain estimates were obtained and averaged for all the beam steering angles. So the demarcated area becomes smaller for larger maximum angles as illustrated in Figs. 5(b) and 5(d). We observe an improvement in the SNR_e for compounded elastograms when compared to the noncompounded elastograms shown in Figs. 2(a) and 2(d). Note that temporal stretching further improves the compounded elastograms with a subsequent increase in the SNR_e.

The SNR_e plotted versus the number of angular elastograms used for compounding is shown in Fig. 6(a) without and Fig. 6(b) with global temporal stretching. The error bars denote the standard deviation of the SNR_e estimates over eight independent experiments, and are presented only for selected data points to improve the clarity of the figure. For each data set, the values of the SNR_e were calculated using the triangular region shown in Fig. 5(b). Larger angular increments effectively reduce the number of angular elastograms used in the compounding process, consequently reducing computational time. However, the improvement in the SNR_e obtained for the larger angular increment (7.5°) is lower than that obtained for the smaller angular increments due to the fewer number of angular data available for compounding. For the transducer used in this study, the angular increment of around 1.5° to 3.75° provides the best tradeoff in image quality versus acquisition time because fewer angular elastograms need to be averaged to obtain similar increases in the SNR_e. Note that the SNR_e curves for the an-

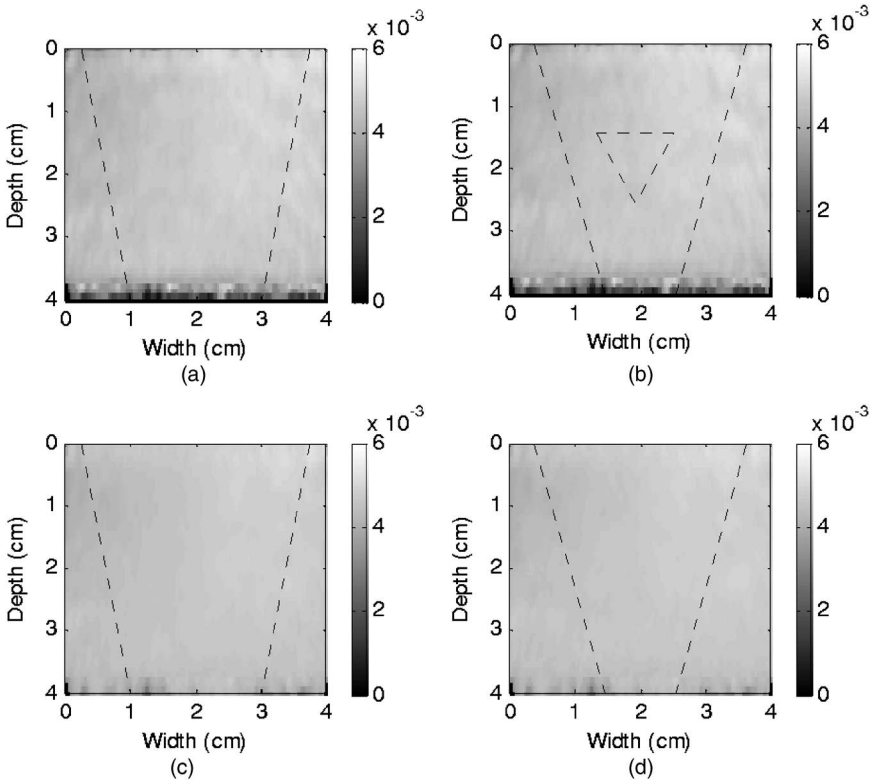

FIG. 5. Compound elastograms obtained (a), (b) without and (c), (d) with global temporal stretching. An angular increment of 1.5° was used over a maximum angle of 10.5° (left) and 15° (right), respectively. Mean and variance of the strain estimates were computed over the triangular region shown on the elastogram (b). The region demarcated by the two dashed lines represents locations common to all angular strain estimates compounded.

gular increment of 0.75° and 1.5° saturate around 25 and 15 angular elastograms, respectively. Since the maximum angle used for compounding can be easily figured out from the angular increment and the number of angular elastograms, the saturation is found to be occurring at a maximum angle of 9°–10.5°. Note also that the SNR_e curves for the angular increment of 3.75° and 7.5° decrease after a maximum angle of around 7.5°. This is due to the increased strain variance of elastograms obtained for the large beam insonification angles, as shown in Fig. 3(b). Figure 6(a) demonstrates an increase in the SNR_e from about 24 dB at 0° to about 29 dB at a maximum angle of 10° for the angular increment of 0.75° or 1.5°. The results obtained with temporal stretching in Fig. 6(b) demonstrate a similar trend, but provide improved SNR_e values.

B. Inclusion phantom

Figure 7 presents elastograms for the single inclusion phantom with and without compounding. The elastograms obtained without temporal stretching are shown in Figs. 7(a)–7(c) and those with temporal stretching are shown in Figs. 7(d)–7(f). The noncompounded elastograms are given in the first column and the compounded elastograms are shown in the second and third column, where an angular increment of 1.5° and maximum angles of 10.5° and 15° were used during spatial angular compounding, respectively. These compounded elastograms demonstrate a significant reduction in noise artifacts and subsequent improvement in the detectability of the inclusion. The boundaries of the inclusion visualized on the compounded elastograms are smoother and

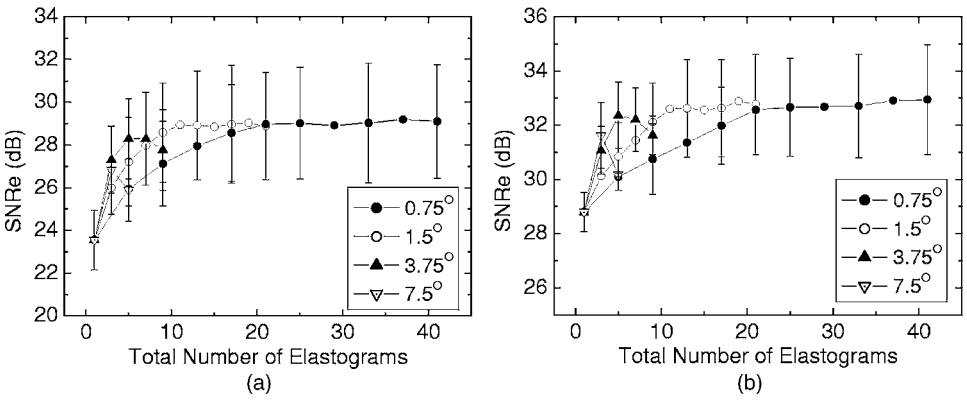

FIG. 6. Mean SNR_e and standard deviation shown as the errorbars of angular compounded elastograms (a) without and (b) with global temporal stretching vs total number of elastograms over which compounding was performed. Results obtained using 0.75°, 1.5°, 3.75°, and 7.5° angular increments are shown.

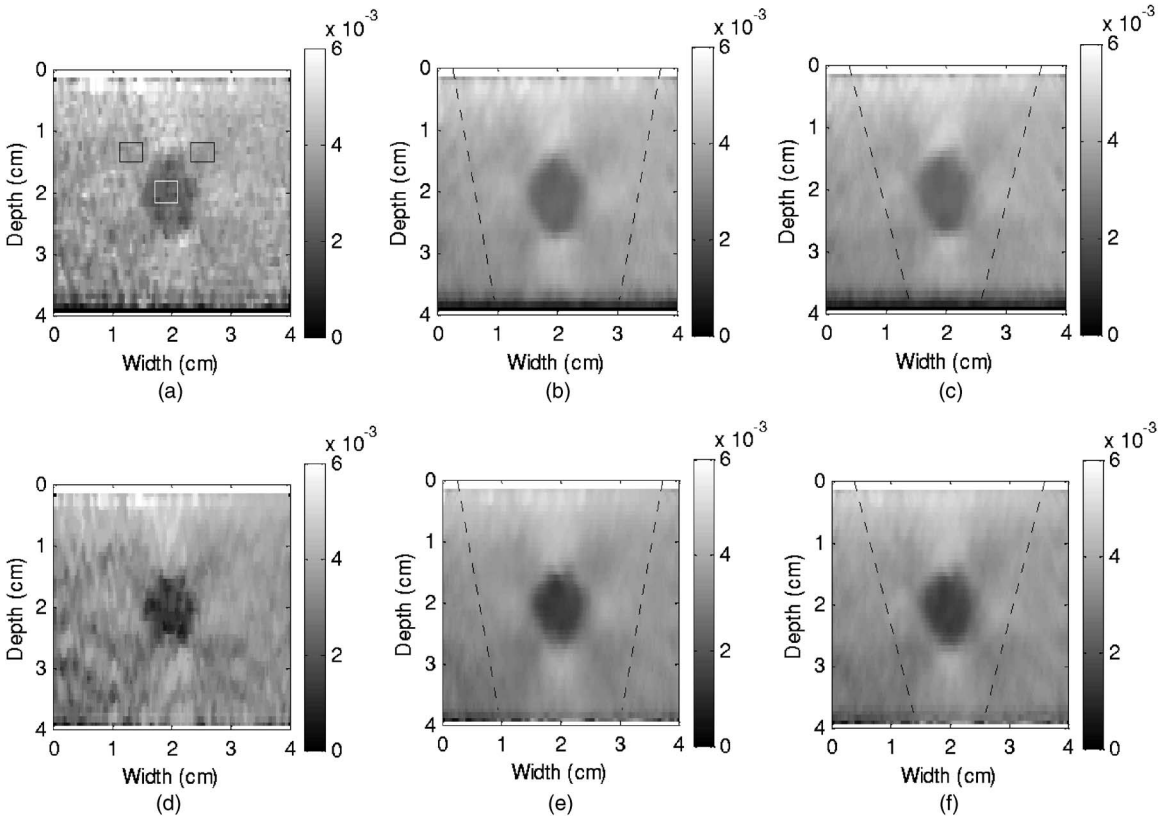

FIG. 7. Elastograms of the inclusion phantom, where the first row illustrates elastograms without global temporal stretching and the second row shows those with global temporal stretching. The first column represents elastograms obtained without compounding and the second and third columns show compounded elastograms using 1.5° angular increments with a maximum angle of 10.5° and 15°, respectively.

better defined than those without compounding. Moreover, global temporal stretching further improves the image quality, as shown in Figs. 7(e) and 7(f). The inclusion appears to be smaller than that observed without temporal stretching. Note that the visual quality of the inclusion in the compounded elastogram using a maximum angle of 10.5° is better than that for the compounded elastogram using a maximum angle of 15°. This is quantified using the contrast and CNR_e parameter plotted and described in Figs. 8 and 9.

Quantitative variations in the strain contrast and CNR_e were calculated using the rectangular ROI within the inclusion and in the background region, as shown in Fig. 7(a). The strain contrast plotted versus the number of angular elastograms used for compounding is shown in Fig. 8(a) without and Fig. 8(b) with temporal stretching. The error bars denote the standard deviation of the mean contrast obtained over eight sets of compounded elastograms. Note that angular compounding has little effect on the strain contrast. We only observe a slight decrease of the strain contrast with an increase in the number of angular elastograms used for compounding for stretching case, as shown in Fig. 8(b).

The CNR_e curves are plotted against the number of angular elastograms used in the compounding process, as shown in Fig. 9. The CNR_e of the compounded elastogram increases with the number of angular elastograms to a maximum CNR_e value, then it slightly decreases with further increasing the

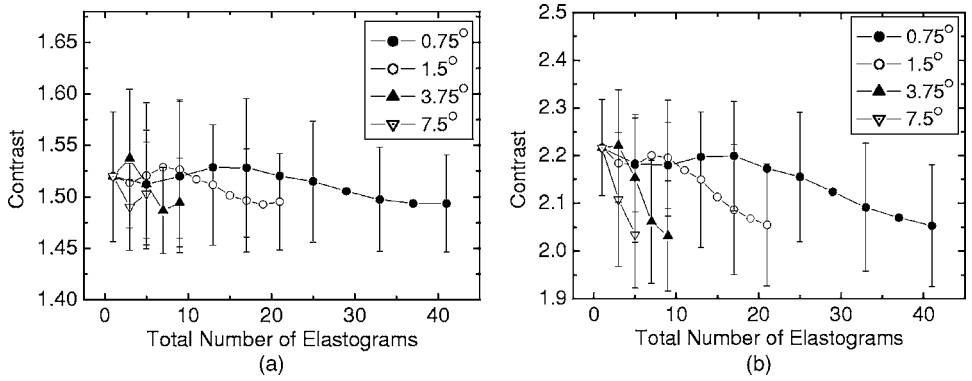

FIG. 8. Plots of the mean strain contrast with standard deviation shown as the errorbars over eight independent realizations of the compounded elastograms (a) without and (b) with global temporal stretching. The strain contrast is plotted vs the number of angular elastograms used for compounding.

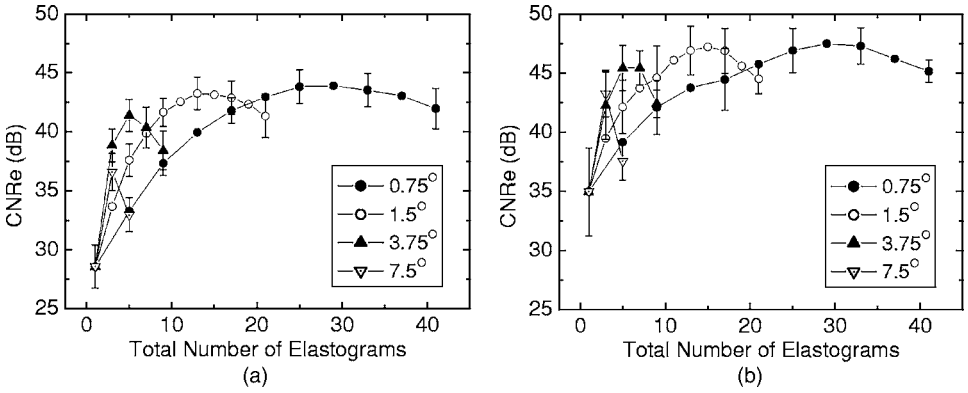

FIG. 9. Plots of the mean CNR_e with standard deviation shown as the errorbars over eight independent realizations of the compound elastograms (a) without and (b) with global temporal stretching vs the number of angular elastograms used for compounding.

number of angular elastograms used for compounding. As shown in Fig. 9(a), the CNR_e increases from 28 to 44 dB for small angular increments (0.75° or 1.5°) over the maximum angle from 0° to 10.5°, providing an improvement of 16 dB. For large angular increments, the increase in the CNR_e obtained by compounding is smaller, as seen in Fig. 9(a), where a 7 dB improvement for the angular increment of 7.5° is observed. On the other hand, the CNR_e with stretching in Fig. 9(b) increases from 35 to 47 dB for small angular increments over the maximum angle from 0° to 10.5°, providing an improvement of 8 dB. And large angular increments provide smaller improvement in the CNR_e. Therefore, the optimum value for the maximum angle used is around 10 deg for our experiment. The angular increment between 1.5 and 3.75 appears to contain the optimum value, which would minimize the number of angular elastograms required for compounding while maintaining similar improvements in the CNR_e.

IV. DISCUSSION

Spatial angular compounding for elastography was initially performed by translating a phased-array transducer as illustrated by Techavipoo *et al.*[22,23] for reduction of noise artifacts and subsequent improvement in the SNR_e and CNR_e. The SNR_e improved by a factor of 2.4 (around 3.8 dB) for maximum angles in the range of 18.75°–30° in experiments with a uniformly elastic phantom. Techavipoo *et al.* also demonstrated a CNR_e improvement of around 8–13 dB, with a maximum angle ranging from 12° to 18.75°, using an inclusion phantom. In this article, we present the experimental results of spatial compounding performed using a linear-array transducer with beam steering. The increase in the SNR_e obtained by angular compounding for the uniform phantom is around 5 dB for maximum angles in the range of 9°–15°. Note that this improvement in the SNR_e was obtained over a smaller maximum angle on the linear-array transducer when compared to that used on the phased-array transducer. The improvement in the CNR_e for the inclusion phantom is around 8–16 dB, with the maximum angles ranging from 9° to 10°. The maximum angle that can be used for the CNR_e improvement is slightly smaller than that of the phased-array transducer case. For both the SNR_e and CNR_e improvement, the linear-array transducer provides significantly larger improvements in the SNR_e and CNR_e than that obtained using the phased-array transducer.

To perform efficient spatial angular compounding, we need to choose an optimum angular increment so that fewer angular elastograms are required to obtain similar improvements in the SNR_e or CNR_e. Angular increments of 0.75°–3.75° provide similar improvements in SNR_e and CNR_e for a fixed maximum angle (see Figs. 6 and 9). This is because rf data from a tissue volume viewed with beams separated by a small angular increment are highly correlated.[33] However, for a smaller angular increment (0.75°), the compounding efficiency is low since a larger number of angular elastograms are required to achieve a given SNR_e or CNR_e level. For a very large angular increment (7.5°), on the other hand, the improvement in image quality is lower than that obtained for the smaller angular increment, due to the fewer number of angular strain data available for compounding. In our experiment, the optimum angular increment lies between 1.5° and 3.75°, which is similar to the results of the phased-array transducer reported in Refs. 22 and 23. The use of this optimum angular increment could reduce the number of angular elastograms that have to be utilized in the compounding process, and hence reduce the computation time. The approach discussed by Trahey *et al.*[34] may be another approach to compute the optimum angular increment directly from the angular elastograms.

For the linear-array transducer used in this study, the beam steering angle is limited to about 15°, which is much smaller than the insonification angle of 45° provided by the phased-array transducer.[22,23] Angular compounding for the angles beyond 15° has not been investigated in this study. However, the experimental results obtained imply that the use of beam steering angle larger than 15° may not further improve the image quality. The SNR_e curves presented in Fig. 6, show saturation around an insonification angle between 9° and 15°. The CNR_e values obtained even decrease after a maximum angle of 10°, as shown in Fig. 9. Results obtained using the phased-array transducer also demonstrate a similar trend.[22,23] In this article, we therefore select the maximum angle to be around 10° beyond which no appreciable increases in the SNR_e or CNR_e are obtained. This can be explained by the significant increase in the decorrelation

of the pre- and postcompression rf echo signals at larger angles. Moreover, the common region (where strain estimates from all angular insonifications are present) in the compounded elastograms becomes smaller when using larger angles, as described in Figs. 5 and 7. If the common region is too small to contain the target to be imaged, the efficiency of the angular compounding becomes lower because the angular data at larger angles would not contribute to the compounded elastogram for imaging the target region. Therefore, in our experience a maximum angle of 10° is large enough to perform angular compounding.

The utilization of beam steering on linear-array transducer greatly improves the efficiency of spatial-angular compounding compared to the use of the phased array transducer. With beam steering, the linear-array transducer is not required to be translated along the lateral direction like the phased array transducer. The angular rf data are also obtained directly using beam steering, without the rearranging of the data required in the previous study.[22,23] Another advantage of using beam steering with linear-array transducers is that the phantom would always be scanned along the same image plane since beam steering is electronically controlled. Translation of the phased-array transducer may lead to the deviation of the image plane from its original position in the elevational dimension when the transducer is mechanically moved on the phantom along the lateral direction. All of these advantages make the linear-array transducers more suitable for spatial-angular compounding for elastography in clinical applications.

As previously illustrated by Techavipoo *et al.*,[22,23] spatial-angular compounding can be applied in conjunction with the global temporal stretching and other algorithms to reduce noise artifacts. The results in this article demonstrate a further improvement in the SNR_e and CNR_e using temporal stretching. For the uniform phantom, global temporal stretching provides very smooth compounded elastograms, as shown in Figs. 5(c) and 5(d). For the inclusion phantom, lesion detectability is also improved with global temporal stretching, but adaptive stretching may provide even better results.

For elastographic applications, angular beam steered data also can be utilized for estimating normal and shear strain tensors in elastography.[35] The Ultrasonix 500RP system and its research interface enabled the use of beam steering on the linear-array transducers to acquire the angular rf data presented in this article. This system provides a suitable platform for evaluation of different algorithms to improve elastographic image quality and implementation of real-time solutions for strain imaging.

V. CONCLUSION

The performance of spatial-angular compounding for elastography is investigated in this article using beam steering on a linear-array transducer. Experimental results demonstrate a significant improvement in both the SNR_e and the CNR_e obtained by spatial angular compounding. The angular increment and the maximum angle used for compounding are two important factors that affect the efficiency of the angular compounding algorithm. The use of an optimal angular increment (between 1.5° and 3.75°) and limiting the maximum angle to around 10° provides the most efficient approach for our experimental setup. Angular compounding can also be used in conjunction with other noise-reduction algorithms, such as temporal stretching as shown in this article. Compared with phased-array transducers, linear-array transducers are more suitable for clinical applications of the spatial compounding technique. The results presented in this study further demonstrate the feasibility of utilizing spatial-angular compounding on clinical scanners for elastography.

ACKNOWLEDGMENTS

This work is supported in part by NIH Grant Nos. R21 EB003853 and R21-EB002722. The authors would also like to thank Dr. Laurent Pelissier for the loan of the Ultrasonix 500 RP system used on this research.

[a]Author to whom correspondence should be addressed. Present address: Department of Medical Physics, The University of Wisconsin-Madison, Madison, WI-53706. Electronic mail: tvarghese@wisc.edu

[1]J. Ophir, I. Cespedes, H. Ponnekanti, Y. Yazdi, and X. Li, "Elastography—A quantitative method for imaging the elasticity of biological tissues," Ultrason. Imaging **13**, 111–134 (1991).

[2]R. Muthupillai, D. J. Lomas, P. J. Rossman, J. F. Greenleaf, A. Manduca, and R. L. Ehman, "Magnetic-resonance elastography by direct visualization of propagating acoustic strain waves," Science **269**, 1854–1857 (1995).

[3]J. Ophir, S. K. Alam, B. Garra, F. Kallel, E. Konofagou, T. Krouskop, and T. Varghese, "Elastography: Ultrasonic estimation and imaging of the elastic properties of tissues," Proc. Inst. Mech. Eng., Part H: J. Eng. Med. **213**, 203–233 (1999).

[4]T. Varghese, J. Ophir, E. Konofagou, F. Kallel, and R. Righetti, "Tradeoffs in elastographic imaging," Ultrason. Imaging **23**, 216–248 (2001).

[5]A. Pesavento, A. Lorenz, S. Siebers, and H. Ermert, "New real-time strain imaging concepts using diagnostic ultrasound," Phys. Med. Biol. **45**, 1423–1435 (2000).

[6]I. Cespedes, J. Ophir, H. Ponnekanti, and N. Maklad, "Elastography: Elasticity imaging using ultrasound with application to muscle and breast *in vivo*," Ultrason. Imaging **15**, 73–88 (1993).

[7]M. O'Donnell, A. R. Skovoroda, B. M. Shapo, and S. Y. Emelianov, "Internal displacement and strain imaging using ultrasonic speckle tracking," IEEE Trans. Ultrason. Ferroelectr. Freq. Control **41**, 314–325 (1994).

[8]K. J. Parker, S. R. Huang, R. A. Musulin, and R. M. Lerner, "Tissue response to mechanical vibrations for 'sonoelasticity imaging," Ultrasound Med. Biol. **16**, 241–246 (1990).

[9]M. Bertrand, M. Meunier, M. Doucet, and G. Ferland, "Ultrasonic biomechanical strain gauge based on speckle tracking," *IEEE Ultrasonics Symposium*, 1989, pp. 859–864.

[10]T. A. Krouskop, D. R. Dougherty, and F. S. Vinson, "A pulsed Doppler ultrasonic system for making noninvasive measurements of the mechanical properties of soft tissue," J. Rehabil. Res. Dev. **24**, 1–8 (1987).

[11]M. F. Insana, L. T. Cook, M. Bilgen, P. Chaturvedi, and Y. Zhu, "Maximum-likelihood approach to strain imaging using ultrasound," J. Acoust. Soc. Am. **107**, 1421–1434 (2000).

[12]K. Nightingale, M. Scott Soo, R. Nightingale, and G. Trahey, "Acoustic radiation force impulse imaging: *In vivo* demonstration of clinical feasibility," Ultrasound Med. Biol. **28**, 227–235 (2002).

[13]A. Pesavento, A. Lorenz, S. Siebers, and H. Ermert, "New real-time strain imaging concepts using diagnostic ultrasound," Phys. Med. Biol. **45**, 1423–1435 (2000).

[14]D. B. Plewes, I. Betty, S. N. Urchuk, and I. Soutar, "Visualizing tissue compliance with MR imaging," J. Magn. Reson Imaging **5**, 733–738 (1995).

[15]S. K. Alam, J. Ophir, and E. E. Konofagou, "An adaptive strain estimator for elastography," IEEE Trans. Ultrason. Ferroelectr. Freq. Control **45**, 461–472 (1998).
[16]S. K. Alam and J. Ophir, "Reduction of signal decorrelation from mechanical compression of tissues by temporal stretching: Applications to elastography," Ultrasound Med. Biol. **23**, 95–105 (1997).
[17]I. Cespedes and J. Ophir, "Reduction of image noise in elastography," Ultrason. Imaging **15**, 89–102 (1993).
[18]T. Varghese, J. Ophir, and I. Cespedes, "Noise reduction in elastograms using temporal stretching with multicompression averaging," Ultrasound Med. Biol. **22**, 1043–1052 (1996).
[19]U. Techavipoo and T. Varghese, "Wavelet denoising of displacement estimates in elastography," Ultrasound Med. Biol. **30**, 477–491 (2004).
[20]P. C. Li and M. J. Chen, "Strain compounding: A new approach for speckle reduction," IEEE Trans. Ultrason. Ferroelectr. Freq. Control **49**, 39–46 (2002).
[21]P. Chaturvedi, M. F. Insana, and T. J. Hall, "2-D companding for noise reduction in strain imaging," IEEE Trans. Ultrason. Ferroelectr. Freq. Control **45**, 179–191 (1998).
[22]U. Techavipoo and T. Varghese, "Improvements in elastographic contrast-to-noise ratio using spatial-angular compounding," Ultrasound Med. Biol. **31**, 529–536 (2005).
[23]U. Techavipoo, Q. Chen, T. Varghese, J. A. Zagzebski, and E. L. Madsen, "Noise reduction using spatial-angular compounding for elastography," IEEE Trans. Ultrason. Ferroelectr. Freq. Control **51**, 510–520 (2004).
[24]C. B. Burckhardt, "Speckle in ultrasound B-mode scans," IEEE Trans. Sonics Ultrason. **25**, 1–6 (1978).
[25]R. R. Entrekin, B. A. Porter, H. H. Sillesen, A. D. Wong, P. L. Cooperberg, and C. H. Fix, "Real-time spatial compound imaging: application to breast, vascular, and musculoskeletal ultrasound," Semin Ultrasound CT MR **22**, 50–64 (2001).
[26]S. K. Jespersen, J. E. Wilhjelm, and H. Sillesen, *Ultrasound Spatial Compound Scanner for Improved Visualization in Vascular Imaging*, Sendai, Japan, 1998 (B-K Med. A/S Gentofte Denmark), pp. 1623–1626.
[27]H. Ping, "Spatial compounding in 3D imaging of limbs," Ultrason. Imaging **19**, 251–265 (1997).
[28]E. L. Madsen, G. R. Frank, T. A. Krouskop, T. Varghese, F. Kallel, and J. Ophir, "Tissue-mimicking oil-in-gelatin dispersions for use in heterogeneous elastography phantoms," Ultrason. Imaging **25**, 17–38 (2003).
[29]F. Kallel and J. Ophir, "A least-squares strain estimator for elastography," Ultrason. Imaging **19**, 195–208 (1997).
[30]Y. C. Fung, *Biomechanics: Mechanical Properties of Living Tissues* (Springer-Verlag, New York, 1981).
[31]T. Varghese and J. Ophir, "A theoretical framework for performance characterization of elastography: The strain filter," IEEE Trans. Ultrason. Ferroelectr. Freq. Control **44**, 164–172 (1997).
[32]T. Varghese and J. Ophir, "An analysis of elastographic contrast-to-noise ratio," Ultrasound Med. Biol. **24**, 915–924 (1998).
[33]P. He, "Spatial compounding in 3D imaging of limbs," Ultrason. Imaging **19**, 251–265 (1997).
[34]G. E. Trahey, S. W. Smith, and O. T. Vonramm, "Speckle pattern correlation with lateral aperture translation—Experimental results and implications for spatial compounding," IEEE Trans. Ultrason. Ferroelectr. Freq. Control **33**, 257–264 (1986).
[35]U. Techavipoo, Q. Chen, T. Varghese, and J. Zagzebski, "Estimation of displacement vectors and strain tensors in elastography using angular insonifications," IEEE Trans. Med. Imaging **23**, 1479–1489 (2004).